JOURNAL OF PROPULSION AND POWER
Vol. 26, No. 6, November–December 2010

Parametric Study of the Generation of Shocks in Near-Critical Turbofan Nozzles

Matthew T. Kube-McDowell,* Anastasios S. Lyrintzis,† and Gregory A. Blaisdell‡
Purdue University, West Lafayette, Indiana 47907

DOI: 10.2514/1.45691

The purpose of this investigation is to identify the factors that contribute to internal shocks in the nozzles of engines operated at high subcritical pressure ratios and determine whether these factors can be controlled through design of the nozzle geometry. A number of parametrically generated nozzle geometries were tested using the computational fluid dynamics solver Wind-US, and the peak Mach numbers in the jet stream and the size and geometry of the shocks were extracted from the computational solutions. Axisymmetric and three-dimensional calculations found that regions of high curvature near the nozzle exit are the strongest factor to contribute to the generation of internal shocks. The strength of these shocks can be controlled by altering the nozzle design to move high-curvature regions upstream without changing the total nozzle length. Shocks can also be weakened and even eliminated by stretching the nozzle axially, reducing the curvature throughout. If a given nozzle profile is extended axially in this manner, there is a monotonic and nearly linear relationship between the length of the nozzle and the thrust it can produce before generating an internal shock. Finally, small corners or rough areas on a nozzle wall in the critical region near the nozzle exit can exacerbate the turning effects that cause internal shocks to form.

Nomenclature

A	=	axially projected shock area, cm^2
II	=	normalized second invariant of velocity gradient tensor
l	=	radial shock length, m
M	=	Mach number
R	=	radial coordinate, in. or m
S_{ij}	=	strain rate tensor
T	=	uninstalled thrust, lbf
u	=	velocity
X	=	jet axis coordinate, in. or m
x	=	position
y_1^+	=	nondimensional first-point offwall grid spacing
α	=	absolute wall angle, degrees
Δ	=	distance from beginning of spline, prefix
Ω_{ij}	=	rotation rate tensor

Subscripts

cp	=	to or at control point
cs	=	across region of cubic spline

I. Introduction

WHEN a typical turbojet or turbofan engine is operated at a high-enough NPR, there is a risk that a portion of the flow will become overexpanded in the nozzle, resulting in a patch of supersonic flow and a shock inside the nozzle. This internal shock can have several negative impacts, including stagnation pressure losses and shock-related noise. Because internal shocks occur at these high NPRs, they are more likely to be observed at high throttle settings and contribute noticeably to jet noise. Since civil aircraft must operate under federal noise limits, internal shocks can limit an aircraft's operational envelope, due to both performance and noise requirements.

Tester and Fisher [1–3] and Garrison et al. [4–9] have been developing a semi-empirical method by which a single, steady-state, Reynolds-averaged Navier–Stokes calculation can be used to predict the far-field acoustic spectra of jet noise very rapidly. The method involves the identification of specific sources of noise, modeling these sources as simplified sources with a known strength and frequency contribution, and appropriately combining these sources into a far-field noise spectrum. Tester and Fisher's [1–3] work focused on using this noise model to predict the acoustics of internally mixed jets with lobed mixers. This research, as well as work by Wright et al. [10], identified a high-frequency noise source believed to result from a turbulent mixing layer between the core and bypass flow interacting with a standing internal shock. This phenomenon is referred to as high Mach number lift (HML) noise. Earlier work by Ribner [11–13] provides a theoretical basis for the enhancement of turbulence passing through a shock, showing the high-frequency contribution to far-field noise. Garrison et al. [4], building on this theoretical basis, developed an expression for the strength of an HML noise source, which has been validated as explaining the difference in magnitude of HML noise contributions between experimental acoustic measurements. While a simple model of the radiation process of HML noise has been proposed by Tester and Fisher [3], the phenomenon of HML noise is not yet fully understood and a noise source model that accounts for an HML noise contribution has yet to be developed.

The findings that prompted this investigation come from this previous research, which in turn was based on a test program conducted in 2003 [14]. Three scale nozzle geometries (designated as L0, L1, and L2, in order of length, with L0 being the longest) were tested for acoustic performance. Operating conditions for these tests were defined by the nozzle pressure ratio (NPR) and nozzle temperature ratio (NTR) for the core and bypass streams. The nozzles were operated at a core NPR of 1.74 and a bypass NPR of 1.82, close to but below the critical NPR of $\approx$1.893; the term *high subcritical* is used later to refer to this range. In both acoustic testing and computational predictions, the L1 nozzle demonstrated little or no internal shock or HML noise at these conditions, while the L0 and L2 results featured prominent shocks and high-frequency noise enhancement.

An example of this internal shock formation is shown in Fig. 1a. Local compression near the wall causes the flow to be accelerated to

Received 27 May 2009; revision received 15 April 2010; accepted for publication 4 August 2010.

*GAANN Fellow, School of Aeronautics and Astronautics. Student Member AIAA.
†Professor, School of Aeronautics and Astronautics. Associate Fellow AIAA.
‡Associate Professor, School of Aeronautics and Astronautics. Associate Fellow AIAA.

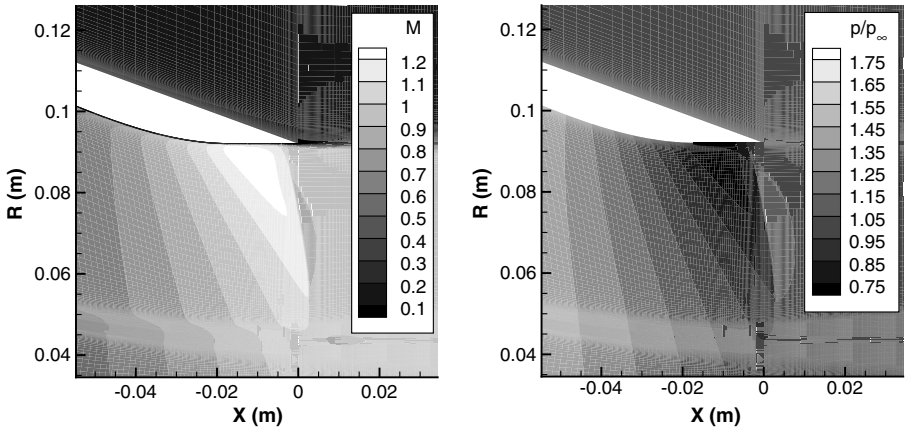

a) Mach number **b) Pressure ratio**

Fig. 1 Contours of a) Mach number and b) pressure ratio in approximate L2 nozzle (ID 2) showing internal shock.

sonic conditions. Downstream of the sonic line, the nozzle wall has a convex curvature, allowing the flow to expand locally and accelerate to supersonic. The interaction between the center of the mixing layer and the region of supersonic flow can be seen from sudden jumps in the Mach contours. Figure 1b plots the pressure near the nozzle exit, normalized by ambient conditions. The flow in the supersonic region is clearly overexpanded, reaching values of p/p_∞ of 0.75 or less. The data for these figures are taken from computational solutions processed in the course of this paper, the details of which are described later.

The work presented in this paper attempts to verify that the discrepancy between the performances of the L0, L1, and L2 nozzles is due to shocks and determine methods of controlling internal shock production through design of the interior nozzle geometry. This is accomplished through several stages of parametric variation of the interior nozzle wall. The first stage varies the nozzle profile in the mixing region of a confluent nozzle with a fixed nozzle length. A fixed profile is then stretched axially to determine if additional length effects are present. The stretched nozzles are then operated under varying inlet conditions to develop guidelines for the tradeoffs for shockless operation. Finally, the results are validated with a grid-resolution sensitivity test and a grid-distribution sensitivity test, and a select set of three-dimensional forced mixer configurations are computed to confirm that the trends observed are applicable to modern bypass nozzle designs. The information on internal shock generation gathered through this investigation is meant to be used in the early stages of design and optimization to help reduce the occurrence and strength of internal shocks and related effects. Preliminary results of this work were presented to the AIAA Aeroacoustics Conference in 2008 [15].

II. Geometry, Parameterization, and Simulation

A. Nozzle Geometry

As mentioned in the previous section, the longest and shortest experimental nozzles (L0 and L2, respectively) suffered from internal shocks at the highest engine setting. The L2 nozzle was chosen as the basis for all experimental nozzle geometries in this investigation for its simpler and smoother design and ease of parameterization.

Although the other two experimental nozzles were not chosen for parametric testing in this investigation, the differences in their test results were useful in determining what factors might influence the generation of internal shocks. It was therefore necessary to examine the geometry of all three experimental nozzles and identify features present in the L1 nozzle that are absent from the other two, or vice versa.

Figure 2 displays the axisymmetric geometry and angles of the interior wall of each of the three experimental nozzles, taken from a database of points developed after the experimental acoustic tests [6]. All three nozzles share a consistent exit area and are aligned in this figure at the nozzle exit. Several obvious differences in the wall angle characteristics can be seen between the experimental nozzles. The L0 and L2 both have higher peak wall angles than the L1, and analyzing the wall angle and geometry together reveals that this also results in a higher rate of area contraction. The L0 also has a secondary peak in wall angle, and this peak and the point of maximum wall angle for the L2 both occur closer to the nozzle exit than the peak wall angle of the L1 does.

B. Nozzle Parameterization

The results from the previous section suggested that useful data would be gathered from this investigation if the axial location of the maximum wall angle and the maximum wall angle itself could be controlled. The question of multiple peaks was deemed too complex for this investigation. A measure of the wall curvature would also have been a useful and meaningful parameter; however, as a free parameter controlling a geometric profile, it is less intuitive than controls on the wall angle. Therefore, while the curvature was not used as a parameter to avoid overdefining the system, it is included in the analysis of the results.

It was noticed that specifying the location and value of the maximum wall angle, in addition to boundary conditions, is sufficient to define a two-segment cubic spline. These three inputs define a control point that can be used to generate a complete nozzle profile with an exact representation, allowing for simple analysis and

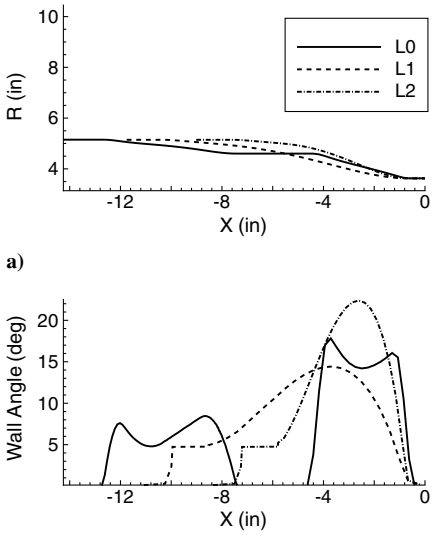

a)

b)

Fig. 2 Experimental nozzle a) axisymmetric geometries and b) wall angles.

arbitrary resolution of any geometry generated. Parameterizing the nozzle with a cubic spline allowed some interesting freedom in defining test cases; for example, by moving the control point toward the exit, the curvature of the nozzle profile near the exit could be increased without changing the maximum angle. It also made parameterizing existing nozzles straightforward, requiring only that the point of greatest wall angle be identified.

The cubic spline was integrated into the L2 nozzle geometry with restrictions designed to maximize the similarity of the ideal conditions between each configuration. The upstream boundary of the spline was set at the axial location of the end of the splitter plate, so that changes in the parametric geometry would have negligible effect on the mixing characteristics. The L2 geometry ends with a short constant-area segment at the nozzle exit, and for consistency and smoothness, the slope of the spline at the downstream end was fixed at zero. Length variations might be achieved by specifying the nozzle length directly; however, with such a model, parameter sets that only vary the nozzle length generate different scaled nozzle profiles, which is undesirable. Therefore, it was decided that length variations would be performed by stretching the nozzle wall geometry by a constant factor, from the inlet to the nozzle exit, to preserve the shape of the parametric region. The mixer and centerbody geometry is held constant to best preserve the mixing properties and frictional losses of the two jets between cases.

Figure 3 demonstrates the process of generating a parametric nozzle geometry. The spline is defined between the end of the mixer splitter plate and the beginning of the constant-area nozzle exit, with the distances ΔX_{cs} and ΔR_{cs} determined by the original geometry. The location of the control point is expressed as a nondimensional distance between the mixer exit plane endpoint and the nozzle exit endpoint ($\Delta X_{cp}/\Delta X_{cs}$ and $\Delta R_{cp}/\Delta R_{cs}$). The sign convention chosen in these distances makes the input parameters more intuitive, as the control point will lie on the diagonal between the two spline endpoints when $\Delta X_{cp}/\Delta X_{cs}$ is equal to $\Delta R_{cp}/\Delta R_{cs}$. The wall angle at the control point (α_{cp}) is then chosen, which fully defines the spline. The exact solution for the spline is digitized at an axial resolution at least as high as the existing geometry database, and those points are rotated, scaled, shifted, and inserted into the database. Finally, if desired, the nozzle geometry is scaled axially by a common nozzle stretching parameter (NSP).

Initial experimentation with this parametric-generation process quickly revealed some limitations. While α_{cp} is a free parameter, too large of an angle results in a nonmonotonic impractical nozzle that is unsuitable for study. Similarly, too small of an angle at the control point causes the maximum wall angle to occur at another point; in the extreme, a small α_{cp} results in two peaks in wall angle similar to the L0 nozzle (as shown in Fig. 2).

To ensure that the free parameter α_{cp} represents a meaningful physical property on a nozzle of practical interest, the inner wall profile must be concave upstream of the control point and convex downstream. An automated tool analyzed the ranges of curvature for the exact spline fits over all possible inputs and produced a map of valid α_{cp} values for all combinations of $\Delta X_{cp}/\Delta X_{cs}$ and $\Delta R_{cp}/\Delta R_{cs}$. It was observed that control points where $\Delta X_{cp}/\Delta X_{cs}$ and $\Delta R_{cp}/\Delta R_{cs}$ were nearly equal, or where the control point was close to the diagonal between the boundary points, had the widest range of acceptable wall angles.

Analysis of the experimental L2 geometry database identified the point of maximum wall angle as corresponding to a value of $\Delta X_{cp}/\Delta X_{cs}$ of 0.62 and a value of $\Delta R_{cp}/\Delta R_{cs}$ of 0.60, with an α_{cp} of close to 23 degrees. To confirm the validity of this approach, the experimental nozzle was compared to this parametric approximation. The exact difference in the approximation was calculated for every database point inside the range of the spline and normalized by the nozzle's exit diameter. The maximum absolute radial deviation from the experimental geometry was only 0.29% of one diameter, with an average absolute deviation of 0.11%.

The control point location for the approximate L2 nozzle was shown by the mapping tool to have a relatively wide range of valid wall angles. The parameters for this approximation ($\Delta X_{cp}/\Delta X_{cs} = 0.62$, $\Delta R_{cp}/\Delta R_{cs} = 0.60$, and $\alpha_{cp} = 23$) were thus chosen as nominal values.

C. Grid Generation

Parametric grids were generated for both axisymmetric flow with a confluent unforced mixer and three-dimensional flow with a moderate-penetration 12-lobe unscalloped mixer. To generate computational domains, the parametric wall geometry for each case was discretized and sliced into existing point databases, replacing the experimental geometry between the mixer exit plane and the nozzle exit. These new points databases were input into MATLAB scripts designed by Garrison et al. [5], modified to meet the expanded needs of this project, which generated two-dimensional surface grids. For three-dimensional configurations, Gridgen was used to generate volume grids over a half-lobe symmetric slice of the nozzle. For parallel processing, axisymmetric grids were divided into six structured computational zones, as shown in Fig. 4; the core inlet, the bypass inlet, the initial mixing area, the nozzle exit, the freestream inlet, and the plume. Three-dimensional grids further split the nozzle exit into two zones and the plume into six zones, for a total of 12. The boundaries of these zones were drawn to minimize skew at difficult locations, such as the end of the centerbody cone, and to minimize discontinuities in the turbulent characteristics between zones.

The scripts build grids based on certain specified constants, such as initial wall spacing, and suggest a grid resolution based on a desired maximum stretching ratio. User-chosen dimensions for each zone are used to define the zone boundaries, and the interior is filled based on the grid spacing of the boundaries. For this paper, grids were generated with a maximum initial wall spacing of 0.5×10^{-6} nozzle diameters and a maximum radial grid stretching ratio of 1.2. For axisymmetric configurations, an estimated shear-layer location is used to cluster points to resolve the shear layer using the wall spacing from the splitter plate as an initial value. Two axisymmetric computations are therefore required for each configuration: one to find the

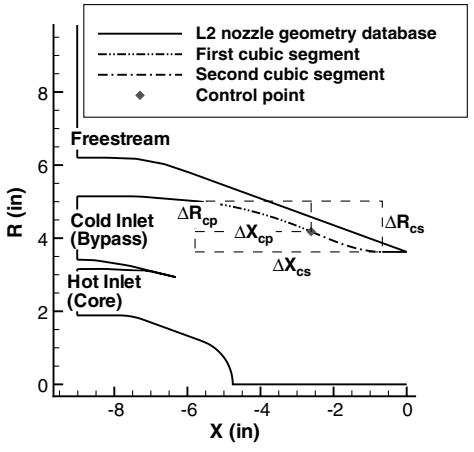

Fig. 3 Schematic of the construction of parametric nozzle from various data sources.

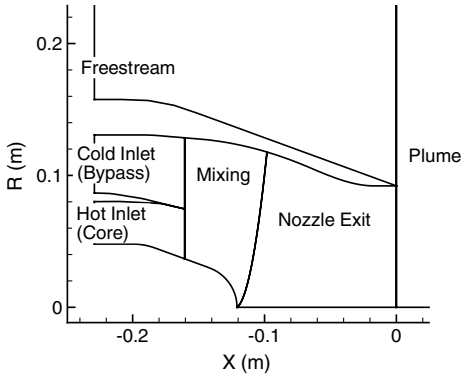

Fig. 4 Computational zones for axisymmetric configurations.

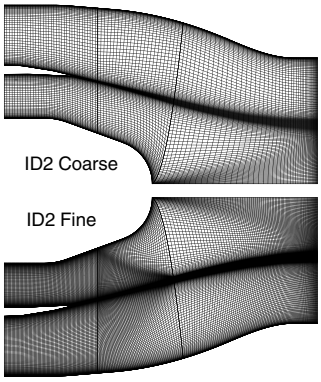

Fig. 5 Representative axisymmetric grids (nozzle interior only) with coarse and fine resolutions.

location and width of the mixing layer and a second computation on a grid refined to that mixing layer.

The typical coarse axisymmetric grid used in this investigation contained approximately 75,000 grid points for the smallest nozzle geometry. Fine axisymmetric grids were also generated, using double the grid points in all directions for grid sizes of at least 300,000 points. Differences in the measured quantities of peak Mach number and projected shock area between the coarse and fine grids were less than 1% for the profile-variation cases, so the fine grid was taken to be sufficiently refined. Three-dimensional grids were generated using the coarse axisymmetric spacing in the axial and radial directions, with at least 2.3 million grid points per configuration. Representative grids showing the difference between these resolutions are shown for the approximate L2 nozzle in Fig. 5.

D. Computational Solver

The computational fluid solver Wind-US [16], version 1, was used to obtain all flow solutions. Wind-US has been validated for use with airbreathing propulsion over a large range of flow Mach numbers [17], and specifically for use with high-speed jets and internal nozzle shocks [18]. Computations were performed using the Reynolds-averaged Navier–Stokes equations and the shear-stress transport (SST) form of the k-ω turbulence model [19] with a conservative second-order-accurate finite difference formulation in space. Computations were performed on a 56-node, 224-processor Linux cluster with 1 GB of RAM per processor. Convergence was measured using the L2-norm residuals of all flow properties, which decreased by at least 3 orders of magnitude during computation, and a monitor of the integrated mass flow through two planes far downstream, which maintained a constant value within 0.5% of its final value. Coarse axisymmetric grids converged in less than a day with a single processor, including intermediate sequenced grid computations, while fine axisymmetric grids required just over a day on four processors. Both grid resolutions were computed for a total of 60,000 iterations, which was more than sufficient for all grids to meet convergence criteria at every level of grid sequencing. Three-dimensional grids converged in between two days and a week on 16 processors, using three levels of grid sequencing, and were computed for a total of 75,000 iterations, sufficient to converge at each sequencing level.

E. Postprocessing

Two common quantities of interest were derived from the solutions in order to compare the performance of each nozzle configuration. The first quantity is the shock strength, measured for the purposes of this paper by the peak Mach number in the flowfield. Second, based on findings from Garrison et al. [4] that suggest a relation between the HML source strength and the projected shock area, the shape of the supersonic region was used to calculate the shock area projected in the direction of the jet axis. The shape of the supersonic region for each solution was captured by finding the points of peak Mach number along each axially directed grid line, isolating the supersonic points, and performing a linear interpolation between the Mach number and the radial coordinate near the endpoints to better approximate the sonic region's exact size. The dimensional uninstalled thrust of the nozzle, in pounds of force, was also computed from conditions at the nozzle exit to validate inlet conditions used in Sec. V. Wind-US postprocessing tools were used for extracting raw data, which were then analyzed using scripts in FORTRAN and MATLAB.

III. Profile Variations

A. Test Matrix

The test matrix for the profile-variation stage consists of five control point locations, each tested at the low and high extremes of wall angle for which they are valid, for a total of 10 trial nozzle configurations. The control points for the test matrix are centered on the approximation of the L2 nozzle and rest approximately on the diagonal of the spline bounding box (see Fig. 3) for the largest range of valid maximum angle values. The nozzle length is held constant from the original L2 geometry. Test points that generated impractical nozzle geometries were not included in the test matrix; in particular, if the control point was placed too far upstream, the resulting geometry would have an unreasonably long region at the nozzle exit with little or no change in nozzle area, and such cases were not tested.

Table 1 lists the input parameters for the test matrix, along with their names and ID numbers. Configuration ID 2 refers to the parametric representation of the original L2 geometry. The list of ID numbers is zero-indexed to clearly delineate between the cases tested in this stage, which are all represented by a single-digit number, and later stages. Coarse- and fine-resolution axisymmetric grids are denoted with C and F, and three-dimensional lobed grids are denoted with 3-D in the text and with 3D in subsequent figures. Additionally, the peak expansion curvature for each configuration is listed in the rightmost column of Table 1, calculated from the analytic representation of the cubic spline. Axisymmetric configurations were tested for all parameters, while three-dimensional testing, because of the increased processor time requirements, was restricted to configurations IDs 0–2 and 5–7.

B. Results

Figure 6 presents the results of the computations. The most significant result, as shown in Fig. 6a, is that the peak Mach number decreases as the point of maximum wall angle moves upstream, and a minimum is not observed within the test matrix. This trend is seen in both low-angle (IDs 0–4) and high-angle (IDs 5–9) nozzle geometries, in coarse- and fine-grid resolutions, and for both axisymmetric and lobed mixers.

One unexpected result is that the high-angle configurations have consistently weaker supersonic patches than their low-angle counterparts. This is counterintuitive, as the high-angle nozzles would be expected to cause stronger turning effects and be less isentropic. However, as an artifact of the method used to generate the cubic spline, the high-angle nozzles have less curvature near the nozzle exit. For the wall angle to reach its maximum value at the control point, the curvature must be discontinuous and flip sign at that point. If the angle at that point is small, the curvature will also be small, and must grow steadily in magnitude toward the exit in order to

Table 1 Table of parameters for profile-variation study

ID	$\Delta X_{cp}/\Delta X_{cs}$	$\Delta R_{cp}/\Delta R_{cs}$	α_{cp}, deg	$(\partial^2 R/\partial X^2)_{max}$, in.$^{-1}$
0	0.42	0.4	23	0.28
1	0.52	0.5	23	0.34
2	0.62	0.6	23	0.44
3	0.72	0.71	23	0.58
4	0.82	0.82	23	0.84
5	0.42	0.4	30	0.21
6	0.52	0.5	30	0.25
7	0.62	0.6	30	0.31
8	0.72	0.71	30	0.43
9	0.82	0.82	30	0.73

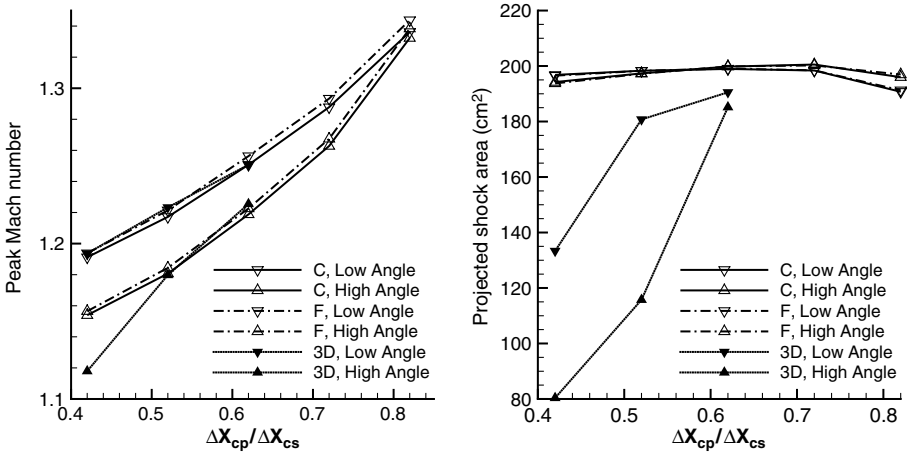

a) Peak mach number **b) Projected shock area**

Fig. 6 Plots of a) shock strength and b) area as a function of axial control point placement.

attain a final angle of zero. A higher peak angle, however, keeps the peak curvature small and farther away from the nozzle exit.

The curvature trend is easily identified when peak Mach number is plotted against the peak expansion curvature of the nozzle, analyzing the low- and high-angle configurations together. This is shown in Fig. 7. The intensity of the internal shock seems to be a turning effect due to curvature near the nozzle exit and can be dampened by moving areas of high curvature upstream toward the mixer. Once again, no minimum was discovered within the test matrix.

As shown in Fig. 6b, the variation in shock size with profile is small for the axisymmetric configurations, compared to the lobed configurations. The total shock area is slightly smaller for weaker shocks, and stronger shocks are generated at more oblique angles to the wall, which decreases their projected area. The mechanism behind the larger variation of the 3-D forced mixing configurations requires closer examination.

The effect of mixing on the shape of the shock is demonstrated in Fig. 8. The three contour plots on the left of the figure display, for the forced mixer approximate L2 configuration (ID 2, 3-D) solution, a normalized second invariant of the velocity gradient tensor, computed in tensor notation as

$$II = \frac{\Omega_{ij}\Omega_{ij} - S_{ij}S_{ij}}{\Omega_{kl}\Omega_{kl} + S_{kl}S_{kl}}$$

where the rotation rate tensor Ω_{ij} and the strain rate tensor S_{ij} are defined as

$$\Omega_{ij} = \frac{1}{2}\left(\frac{\partial u_i}{\partial x_j} - \frac{\partial u_j}{\partial x_i}\right) \qquad S_{ij} = \frac{1}{2}\left(\frac{\partial u_i}{\partial x_j} + \frac{\partial u_j}{\partial x_i}\right)$$

This normalization results in a value that is close to 1 where rotation dominates the velocity gradient, close to -1 where strain dominates, and close to 0 where the two are comparable, such as in shear layers, making it a useful value to visualize the development of vortices. Here, the vortices are displayed on three axial planes; the mixer exit, an intermediate location inside the mixing area, and inside the supersonic region near the nozzle exit. A contour of the peak Mach number contours along each axially directed grid line is displayed alongside the supersonic slice of the second invariant, and the asymmetry in the supersonic region is clearly correlated with the mixing vortex, particularly in the core of the vortex. Near the wall, where the peak Mach number occurs, the flow is relatively undisturbed, and the peak Mach number is mostly consistent between the axisymmetric and lobed configurations. These results suggest that, while the flow nearest the nozzle wall is consistent between the two configurations, the increased mixing causes flow near the edge of the supersonic patch to equalize with the nearby subsonic flow and reduces the overall size of the shock. This is to be expected, as an ideal, fully mixed, high subcritical NPR flow should experience no sonic flow or shocks at all.

Several more subtle variations are also observed in the collected data. Among them is that the predicted thrust increases slightly as the control point moves upstream, or as the peak Mach number decreases. This suggests a small reduction in losses, presumably from the shock being weakened, inside the nozzle.

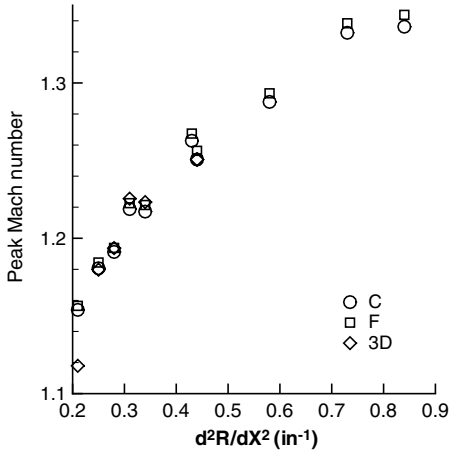

Fig. 7 Profile-variation peak Mach number as a function of peak expansion curvature.

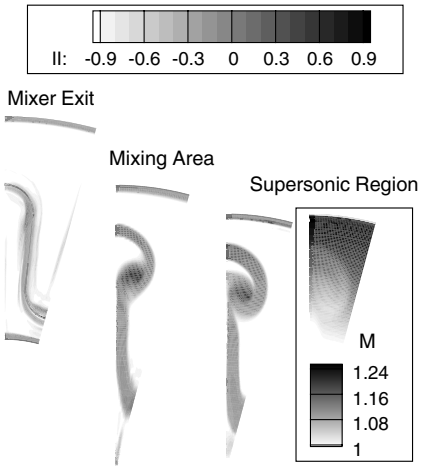

Fig. 8 Downstream progression of normalized second invariant of the velocity gradient tensor for the ID 2 3-D case, demonstrating the effect on the shape of the three-dimensional supersonic region.

IV. Length Variations

This stage of the investigation alters the nozzle geometry by stretching it axially. The motivation for this trial is to confirm and expand upon the findings of the profile-variation trial. Furthermore, data exist for the intermediate-length L1 nozzle (which demonstrated little or no HML noise in the acoustic experiments) and can be used to draw conclusions when compared to a stretched L2 nozzle of the same length.

A. Parametric Variation

The simplest method to generate a stretched nozzle profile is to designate an NSP. The existing geometry database is shifted so that the entry plane is zero in the axial dimension, and then the axial position of each point is multiplied by the NSP. This stretching decreases both the peak wall angle and the peak wall curvature of the nozzle and increases the mixing length of the two engine streams.

It should be noted that the L2 nozzle, which is the basis for all of the parametric geometries in this study, has a small wall angle at the beginning of the spline, which is at the same axial location as the end of the splitter plate. As a result, when the nozzle is stretched, the ratio of the two mixer outlet areas changes slightly. However, the change is determined to be negligible in the context of the trends being observed and preferable to changes in the scaled shape of the nozzle profile.

Since 10 configurations were generated in the profile-variation study, given the ID numbers 0 through 9, it was convenient to denote the axial stretching configurations with the ID numbers 11 through 21, with the ID number being 10 times the NSP for that configuration (ID 11 is stretched by a factor of 1.1, and so forth). ID 10 is never used; the results for an unstretched case are taken from the appropriate solution completed in the previous study.

Coarse- and fine-resolution axisymmetric grids and three-dimensional lobed grids were generated for each length parameter using the experimental geometry database [6], denoted with C, F, and 3-D, as before. In addition, a second fine-resolution grid was generated using the cubic spline parametric representation, which, due to its arbitrary resolution, generated grids with significantly smoother solid-surface boundaries. The cubic spline grids are thus referred to as smooth grids and are denoted with S.

B. Results

Figure 9a shows the strength of the shock as a function of the stretching parameter. As expected, a monotonic decrease in the peak Mach number is shown as the nozzle is stretched axially. This decrease is roughly linear, and does not taper off as the supersonic patch disappears. A long enough nozzle can eliminate the internal shock completely in all cases. As with the profile variation, the behavior of the forced mixer configurations is not qualitatively different from that of the axisymmetric configurations, although the effect of increased mixing length is greater for forced mixers.

The axial stretching of the nozzle geometry also results in a decrease in peak wall angle and curvature. As described in the Introduction, the longest and shortest experimental nozzles (the L0 and L2, respectively) both had prominent internal shocks, while the midlength nozzle (the L1) had the weakest, smallest shock. Comparing these two results suggests that pure nozzle length, or mixing length, is not a relatively strong factor in the generation of internal shocks. This trend can also be compared to the results of the profile variation, where an increase in peak wall angle and a decrease in curvature reduced the strength of the shock generated. The axial stretching results, where both wall angle and curvature decrease, suggest that the effect of the curvature is much stronger than that of the angle.

The projected shock area is shown in Fig. 9b. In the axisymmetric configurations, the area remains relatively constant before declining steadily as the NSP increases. The forced mixer configuration, however, experiences a rapid decrease in the shock area near the nominal nozzle length. This is most likely due to the mixing effect discussed in the profile-variation results. The rapid decrease in shock area is not sustained across the entire test matrix because, as the nozzle is stretched, the supersonic patch becomes limited to the region close to the nozzle wall and forced mixing has less of an effect in this region.

It should also be noted that the percentage errors between the fine and coarse grids is much greater for the length-variation investigation than for the profile-variation cases. In particular, while the peak Mach numbers are still within an acceptable tolerance of 5%, there are larger differences in the estimated shock-termination locations. Additional grid sensitivity studies with long nozzles may be useful to further support these findings.

The difference in smoothness between the two geometry databases impacts the qualitative nature of the internal shock. The S-grid solutions each contain a single peak in Mach number as before. In contrast, the solutions to the C and F grids, generated with the experimental geometry database, each contain a secondary peak in Mach number just upstream of the other. Between the two peaks the flow remains supersonic. Figure 10 shows a typical Mach number contour for an F grid, with a narrow contour level window and alternating bands removed for clarity. The circled regions near the wall clearly demonstrate the two separate peaks in Mach number.

Close examination of the grids generated with the two different databases reveals that the experimental database has a coarser resolution, and sharper turns at database points, near the nozzle exit. These sharper turns appear to exacerbate turning effects, resulting in additional overexpansion that forms the upstream peak Mach number. In addition, the overall peak Mach number observed in F-grid solutions is consistently larger than that observed in S-grid solutions.

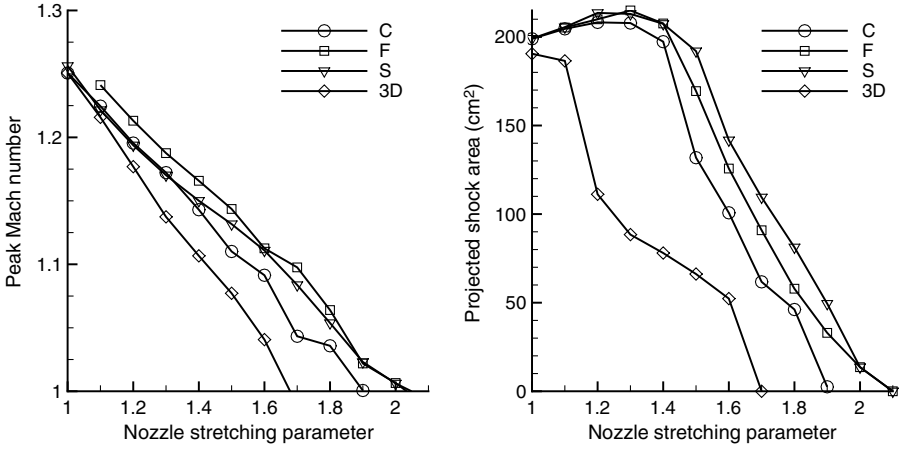

a) Peak mach number **b) Projected shock area**

Fig. 9 Plots of a) shock strength and b) area as a function of stretching parameter.

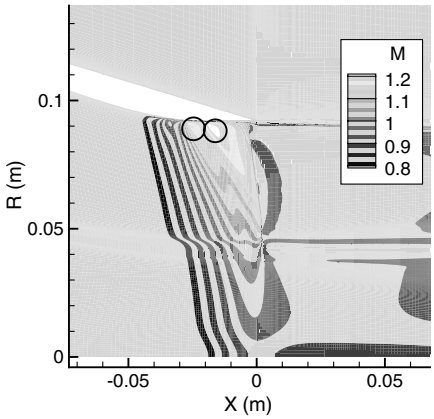

Fig. 10 Mach contour detail of the ID 12-F solution, showing double-peak supersonic structure.

C. Effects of Shape

Extended with an NSP of 1.3, the L2 nozzle is approximately as long as the standard L1 nozzle. To further examine the effects of nozzle shape without the variable of length, a solution for the L1 nozzle was also computed with a fine-grid axisymmetric configuration and compared to the ID 13 configuration.

As shown in Table 2, all three axisymmetric solutions for the extended ID 13 configuration consistently predict a larger, stronger shock than the L1 nozzle solution. Using the fine-grid data as a guide, the L1 performance lies somewhere between that of the 1.5 and 1.6 stretching-parameter cases, whose nozzles are significantly longer. Analyzing the geometry of each profile reveals that the L1 nozzle has a smaller peak curvature near the nozzle exit. This difference supports the conclusion of the parametric profile-variation study suggesting that areas of high curvature near the nozzle exit plane induce turning effects and internal shocks.

V. Shockless Design Tradeoffs

Previous sections have shown that a given nozzle profile can be modified to reduce the intensity of internal shocks. A given nozzle can also be stretched axially to soften internal shocks, although this will incur a weight penalty. It is also possible that modification will not completely prevent an internal shock, or that modification of a nozzle may be limited by manufacturing ability. In such cases, if completely shockless operation is a necessity, either the nozzle must be stretched or the engine must be throttled down from near-critical operation, and an understanding of the nature of the tradeoff between these two options will be helpful in making that decision.

A. Parametric Variation

For this investigation, the relevant parameter is some measure of how the inlet pressure and temperature ratios are reduced compared to a base high subcritical inlet condition. Altering this parameter should realistically vary the inlet conditions. Measurements taken during the related acoustic tests suggest that, at different power settings, the pressure ratio of the two inlet streams and the temperature ratio of the core hot stream vary roughly proportionally with each other, while the temperature ratio of the bypass cold stream remains approximately constant. The parametric variations are thus defined by scaling the core NPR, the bypass NPR, and the core NTR by a fixed amount, which is referred to as the engine setting parameter (ESP). Parametric inlet conditions are generated in one-percent steps. Linear interpolation is used to determine the ESP that produces no shock at each NSP.

Table 2 Quantitative L1 nozzle performance and comparison with stretched L2 nozzles

ID	M_{max} [a]	A, cm^2 [b]
L1	1.133	161.4
13-C	1.172	207.8
13-F	1.188	214.9
13-S	1.170	213.0

[a]Peak Mach number. [b]Projected shock area.

B. Results

Figure 11a shows a monotonic and nearly linear tradeoff between the length of the nozzle and the ESP at which no shock is generated. The choice of implementation of the engine setting parameter is also validated by Fig. 11b, which shows that the engine setting parameter and the predicted thrust from those inlet conditions are almost linearly related. These data suggest a simple monotonic relation between thrust and weight penalties for shockless operation.

VI. Viscous Effects

The parametric variations revealed that the development of internal shocks is highly dependent on turning effects near the nozzle wall. It is worth investigating how dependent this phenomenon is on viscous effects and how fine a resolution is required for computational purposes.

A. Inviscid Solution

To gauge the importance of viscous effects, the ID 2 F grid (ID 2-F) was recomputed with an inviscid Euler solver and slip conditions on the solid walls. As shown in Fig. 12, the internal shock is shown in this case, even without a viscous boundary layer. This confirms that the turning effects that cause internal shocks are a largely inviscid process.

B. Boundary-Layer Resolution

When analyzing the computational results, it was discovered that the default initial wall spacing being used by the grid generation script was insufficient to properly resolve the boundary layer. The typical case would see y_1^+ values between 5 and 10 on the fine-resolution grid, whereas the SST turbulence model requires a value close to 1 to properly handle the development of turbulence in the boundary layer. However, the shocks being studied typically terminate outside of the boundary-layer or mixing-layer regions, requiring a relatively fine-grid resolution there to capture the shock, and increasing the number of grid points to meet both demands at once incurs a computational cost, particularly for the three-dimensional grids, which were based on the coarse-resolution axisymmetric grids. Rather than refine every grid to enforce a peak y_1^+ of 1, it was instead decided to examine two y_1^+-resolved cases and determine whether the quantitative properties being measured and their trends are significantly dependent on the resolution of the turbulent boundary layers.

To maximize the visibility of any changes in the solution due to the change in grid distribution, the profile-variation and length-variation geometries with the strongest shocks were chosen. Since the shockless design variations result in flowfields without any supersonic flow, rendering most of the measured properties zero or meaningless, they were omitted from this investigation.

The two configurations chosen were ID 4, the strongest shock of the profile variations, and ID 11, the shortest nozzle and strongest shock of the length variations. For consistency, the grid sizes of the y_1^+-resolved grids were unchanged from the standard grids, with the improved boundary-layer resolution achieved through redistributing grid points closer to all solid walls. The fine-resolution grids were used as the basis for this test.

Table 3 shows the difference between the original fine-grid solutions (denoted with F) and the y_1^+-resolved grid solutions (denoted with Y). The only significant difference is seen in the measurement of the radial shock-termination location (R_{min}) and in related derived quantities like the shock area. The shock-generation location does not change, suggesting that in either case the grid near the wall is sufficiently resolved to capture the shock generation, regardless of how well the boundary layer is resolved, and that the

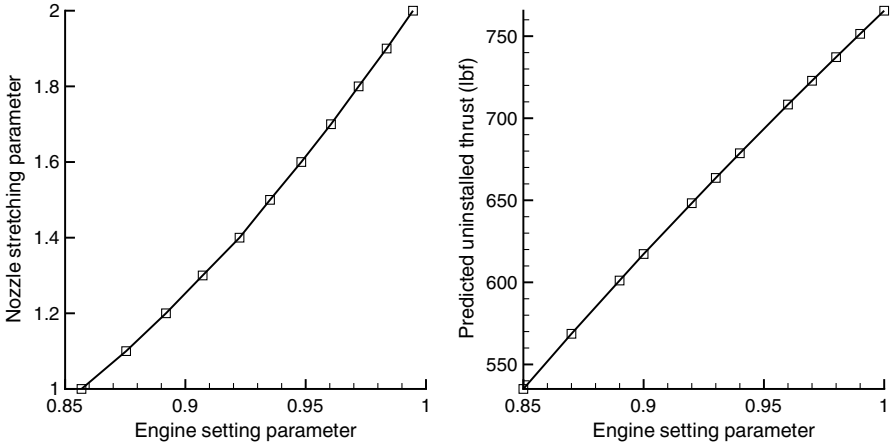

a) Stretching parameter **b) Uninstalled thrust**

Fig. 11 Stretching parameter required for a) shockless operation and b) predicted uninstalled thrust as a function of ESP.

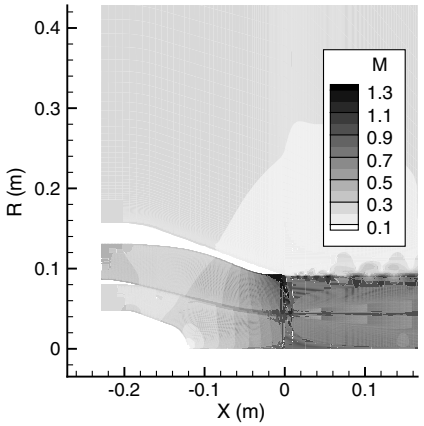

Fig. 12 Mach contours in Euler solution of the ID 2-F configuration.

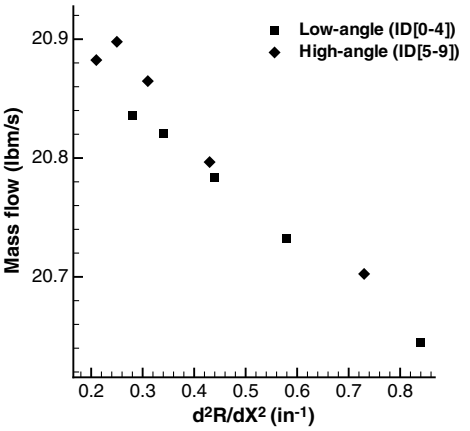

Fig. 13 Mass flow as a function of peak curvature.

shock structure is unaffected by the boundary-layer resolution. The conclusion is made that the difference in the shock-termination location is due to grid resolution in that region, and that the coarser boundary-layer resolution is sufficient for this investigation.

C. Boundary-Layer Development

A nozzle with low curvature was found to be desirable for reducing the strength and size of internal shocks. However, low curvature in a nozzle wall is also known to have a less favorable pressure gradient. This can result in increased growth of boundary layers and reduced mass flow. To examine whether this effect was found in the computed flow solutions, an integrated mass flow across the nozzle exit plane was calculated for the fine-grid axisymmetric profile-variation cases (IDs 0-F–9-F). Additionally, the nozzle exit velocity profiles for three of these solutions (ID 0-F, ID 2-F, and ID 4-F) were plotted together to look for changes in the boundary-layer profile.

Figure 13 shows the mass flow at the nozzle exit plane plotted against the peak expansion curvature for case IDs 0-F–9-F. Smaller values of peak curvature appear to be associated with greater mass flows. Figure 14 shows the velocity profiles in the region near the nozzle wall. The plot area was limited to the boundary-layer region, as the differences in shock placement between these three cases caused substantially different velocity profiles far away from the nozzle wall. The three cases appear to have about the same boundary-layer thickness, but the configuration with the least curvature, ID 0-F, has the fullest velocity profile in the boundary layer, suggesting that reducing the curvature benefits the boundary layer. These cursory results are promising, although a detailed examination of the boundary layer is outside the scope of this paper.

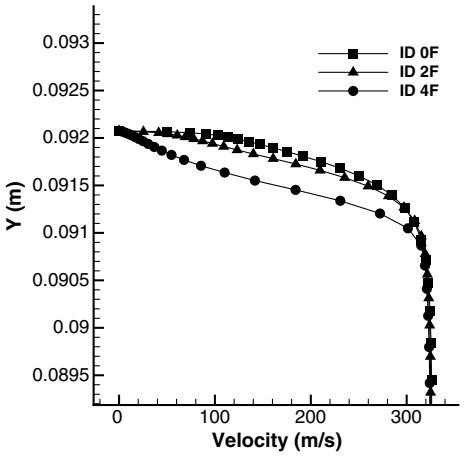

Fig. 14 Detail of nozzle exit velocity profile for select cases.

Table 3 Effect of y_1^+ optimization on measured results

	M_{max}	R_{min}, m[a]	R_{max}[b]	T, lbf	A, cm^2
ID 4-F	1.3438	0.0488	0.0920	751.00	191.2760
ID 4-Y	1.3458	0.0478	0.0920	750.55	194.3463
Error	0.15%	−2.13%	0.00%	−0.06%	1.58%
ID 11-F	1.2216	0.0437	0.0919	761.45	205.5393
ID 11-Y	1.2223	0.0426	0.0919	760.22	208.5785
Error	0.06%	−2.62%	0.00%	−0.16%	1.46%

[a]Radial shock-termination location. [b]Radial shock-generation location.

VII. Conclusions

The aim of this investigation was to determine whether the generation of shocks inside the nozzle of a turbofan engine operating at high subcritical NPRs can be controlled or eliminated by changing the geometry of the nozzle wall. Nozzle geometries were parametrically generated, varying the maximum wall angle, maximum wall curvature, and length. Computational grids with these nozzle configurations were generated with a confluent mixer and simulated at near-critical pressure ratios. To determine the performance tradeoffs for shockless operation, a number of reduced pressure ratio inlet conditions representing lower engine output were also tested. computational fluid dynamics (CFD) cases representing these variations were computed using the CFD solver Wind-US and information about the Mach number and location of any supersonic flow was extracted from the solution.

The data suggest that the generation of internal shocks can be controlled through careful design of the interior nozzle wall geometry. Areas of high curvature near the nozzle exit seem to result in overexpansion that causes shocks to form on the nozzle wall at near-critical NPRs, and the data further suggest that this is a primarily inviscid phenomenon. The parametric nozzle profile variations demonstrate that the strength of those shocks can be reduced by redistributing curvature upstream. A nozzle designed for reduction of internal shocks would place the greatest area contraction closer to the mixer exit plane and terminate the nozzle with a smooth and gradual transition to a constant-area exit.

A longer nozzle can also be used to reduce the appearance of internal shocks. Stretching an engine nozzle axially reduces the wall curvature over the whole length, although it incurs a weight penalty. An internal shock can be completely eliminated by this technique even if the internal nozzle wall profile is already optimized to minimize shock generation or to balance shock generation and other performance concerns. Longer nozzles can also be operated at higher NPRs without generating shocks. The relationship between the nozzle length and the available stand thrust without generating a shock is a linear tradeoff.

The trends and design guidelines observed in this investigation are believed to be valid for internally mixed nozzles with either axisymmetric splitter plates or lobed forced mixers. Forced mixers decrease the size of internal shocks in comparison to axisymmetric splitter plates, but have no additional effect on the strength of the shock. The results of this paper are also consistent with observations of acoustic tests [14] on forced mixer nozzles. Furthermore, since the type of mixing has a negligible effect on the strength of the shock, we expect that these results are also applicable to single jet or separate flow nozzles with near-critical pressure ratios and regions of high convex curvature near the nozzle exit.

The trends found in this paper can be applied to nozzle design to reduce or eliminate internal shocks, improving the acoustic performance of an engine in general and addressing HML noise in high-near-critical NPR flows in particular. An HML-noise-resistant nozzle will have a reasonable mixing length and low expansion curvature on the interior nozzle wall near the exit. Optimization for internal shock generation is expected to be possible even when operating under strict weight limits by simply redesigning the interior nozzle profile.

Acknowledgments

Many thanks to Stephen Heister and the whole faculty and staff of the Purdue Aeronautics and Astronautics department, who have been nothing but supportive. Acknowledgements to Loren A. Garrison of Rolls-Royce Indianapolis, whose work was instrumental to the basis of this project and who was an active participant in the early stages of this investigation, and Brian J. Tester, whose input and guidance were invaluable. M. T. Kube-McDowell was supported by a Graduate Assistance in Areas of National Need (GAANN) Fellowship during the course of this project.

References

[1] Tester, B., and Fisher, M., "A Contribution to the Understanding and Prediction of Jet Noise Generation by Forced Mixers," 10th AIAA/CEAS Aeroacoustics Conference, AIAA Paper 2004-2897, Manchester, England, U.K., May 2004.

[2] Tester, B., and Fisher, M., "A Contribution to the Understanding and Prediction of Jet Noise Generation by Forced Mixers: Part II Flight Effects," 11th AIAA/CEAS Aeroacoustics Conference, AIAA Paper 2005-3094, Monterey, CA, May 2005.

[3] Tester, B., and Fisher, M., "A Contribution to the Understanding and Prediction of Jet Noise Generation by Forced Mixers: Part III Applications," 12th AIAA/CEAS Aeroacoustics Conference, AIAA Paper 2006-2542, Cambridge, MA, May 2006.

[4] Garrison, L. A., Dalton, W. N., Lyrintzis, A. S., and Blaisdell, G. A., "Investigations Of Extensions of the Four-Source Method for Predicting Forced Mixer Jet Noise," 9th AIAA/CEAS Aeroacoustics Conference, AIAA Paper 2003-3165, Hilton Head, SC, May 2003.

[5] Garrison, L. A., Dalton, W. N., Lyrintzis, A. S., and Blaisdell, G. A., "On the Development of Semi-Empirical Noise Models for the Prediction of the Noise from Jets with Internal Forced Mixers," 10th AIAA/CEAS Aeroacoustics Conference, AIAA Paper 2004-2898, Manchester, England, U.K., May 2004.

[6] Garrison, L. A., Lyrintzis, A. S., Blaisdell, G. A., and Dalton, W. N., "Computational Fluid Dynamics Analysis of Jets with Internal Forced Mixers," 11th AIAA/CEAS Aeroacoustics Conference, AIAA Paper 2005-2887, Monterey, CA, May 2005.

[7] Garrison, L. A., Lyrintzis, A. S., and Blaisdell, G. A., "RANS-Based Noise Predictions of Jets with Internal Forced Mixers," 12th AIAA/CEAS Aeroacoustics Conference, AIAA Paper 2006-2599, Cambridge, MA, May 2006.

[8] Garrison, L. A., Dalton, W. N., Lyrintzis, A. S., and Blaisdell, G. A., "Semi-Empirical Noise Models for Predicting the Noise from Jets with Internal Forced Mixers," *International Journal of Aeroacoustics*, Vol. 5, No. 2, April 2006, pp. 139–171. doi:10.1260/147547206777629862

[9] Garrison, L. A., "Computational Fluid Dynamics Analysis and Noise Modeling of Jets with Internal Forced Mixers," Ph.D. Thesis, Purdue Univ., West Lafayette, IN, May 2006.

[10] Wright, C. W., Blaisdell, G. A., and Lyrintzis, A. S., "Investigating Correlations Between Reynolds-Averaged Flow Fields and Noise for Forced Mixed Jets," *Journal of Aircraft*, Vol. 43, No. 4, July–Aug. 2006, pp. 886–894. doi:10.2514/1.12555

[11] Ribner, H. S., "Convection of a Pattern of Vorticity Through a Shock Wave," NACA TR-1164, 1954.

[12] Ribner, H. S., "Shock-Turbulence Interaction and the Generation of Noise," NACA TR-1233, 1955.

[13] Ribner, H. S., "Spectra of Noise and Amplified Turbulence Emanating from Shock-Turbulence Interaction," *AIAA Journal*, Vol. 25, No. 3, March 1987, pp. 436–442. doi:10.2514/3.9642

[14] Bridges, J., and Wernet, M., "Cross-Stream PIV Measurements of Jets with Internal Lobed Mixers," 10th AIAA/CEAS Aeroacoustics Conference, AIAA Paper 2004-2896, Manchester, England, U.K., May 2004.

[15] Kube-McDowell, M., Lyrintzis, A., and Blaisdell, G., "Parametric Study of the Generation of Shocks in Near-Critical Turbofan Nozzles," 14th AIAA/CEAS Aeroacoustics Conference, AIAA Paper 2008-2984, Vancouver, BC, Canada, May 2008.

[16] Wind-US, Software Package, Ver. 1, NPARC Alliance, 2007, http://www.grc.nasa.gov/WWW/RT/2004/RT/RTL-towne.html [retrieved 11 Nov. 2008].

[17] Slater, J. W., Dudek, J. C., and Tatum, K. E., "The NPARC Alliance Verification and Validation Archive," 2000 Fluids Engineering Summer Conference, American Society of Mechanical Engineers Paper 2000-FED-11233, Boston, June 2000.

[18] Hamed, A., and Mohamed, A., "Assessment of Shock Induced Flow Separation and Mixing Layer Predictions in Nozzles and High Speed Jets," 39th AIAA Aerospace Sciences Meeting and Exhibit, AIAA Paper 2001-0225, Reno, NV, Jan. 2001.

[19] Menter, F. R., "Two-Equation Eddy-Viscosity Turbulence Models for Engineering Applications," *AIAA Journal*, Vol. 32, No. 8, Aug. 1994, pp. 1598–1605. doi:10.2514/3.12149

F. Liu
Associate Editor